ACS Photonics
Article
pubs.acs.org/journal/apchd5

In Situ Fabrication of Bendable Microscale Hexagonal Pyramids Array Vertical Light Emitting Diodes with Graphene as Stretchable Electrical Interconnects

Liancheng Wang,[†,‡] Jun Ma,*[,†] Zhiqiang Liu,[†] Xiaoyan Yi,*[,†] Hongwei Zhu,*[,§] and Guohong Wang[†]

[†]Semiconductor Lighting Technology Research and Development Center, Institute of Semiconductors, Chinese Academy of Sciences, Beijing 100083, China

[§]School of Materials Science and Engineering, Center for Nano and Micro Mechanics (CNMM), Tsinghua University, Beijing 100084, China

[‡]Luminous! Center of Excellence for Semiconductor Lighting and Displays, School of Electrical and Electronic Engineering, Nanyang Technological University, 639798 Singapore

S Supporting Information

ABSTRACT: Gallium-nitride (GaN)-based hexagonal pyramids array vertical light emitting diodes (HPA VLEDs) have been assembled through compatible and rationally designed semiconductor fabrication processes. Compared with regular VLEDs (R-VLEDs), the HPA VLEDs have intrinsic bendability and showed a ~56% improvement in internal quantum efficiency (IQE) and a ~52% improvement in light extraction efficiency (LEE). Time-dependent photoluminescence (TDPL) tests and ray tracing simulations confirmed their improved IQE and LEE, respectively. Furthermore, HPA VLEDs with multilayer graphene (MLG) as the electrical interconnects were able to be locally bent and exhibited a stable optical output after many cycles of bending. To obtain uniform microscale HPA, a "dislocation engineering" approach was conceptually demonstrated. The proposed scheme was established for simple materials and low cost engineering; it will guide the fabrication of flexible optoelectronics, especially flexible inorganic GaN-based LEDs.

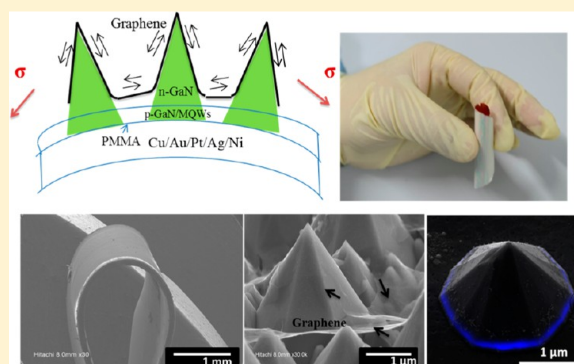

KEYWORDS: *gallium-nitride (GaN), flexible, MOCVD, wet etching, dislocation engineering approach, pattered sapphire substrate, vertical light emitting diodes*

In recent years, flexible electronics and optoelectronics have been extensively investigated.[1−3] They can be transported and integrated into curvilinear surfaces, leading to more sophisticated applications, such as biomedical implants or electronics embedded in clothing,[4] solar-powered electronic textiles, sensors,[5] rollable solar cells,[6,7] panels for portable devices, and so on. Additionally, progresses in light emitting diodes (LEDs), especially GaN-based LEDs, have paved the way for applications in areas ranging from consumer electronics to energy-efficient lighting.[8−10] Flexible LEDs[11−16] could undoubtedly expand applications in flexible TV displays, flexible electronic books, and other potential uses that have not yet been imagined. The appeal of this technical approach is that the properties of LEDs, such as the life span, brightness, and efficiency, exceeds those of currently available organics LEDs (OLEDs). However, conventional GaN-based LEDs are manufactured on rigid sapphire or silicon substrates, interconnected by bulk wire bonding and packaged in a pin or surface-mounted style; therefore, they are less able to bear exceptional levels of mechanical deformability. This rigidity undoubtedly limits their usage as flexible lighting sources.

Based on their advantages of better current injection and heat dissipation, GaN-based vertical-injection LEDs (VLEDs), fabricated through the removal of insulating sapphire substrates and transfer to new metal substrates, have received significant attention.[17−19] In this work, we present some new concepts and approaches for flexible LEDs and report bendable inorganic GaN-based VLEDs for the first time: (1) The fabrication processes involve in situ thinning of the transferred metal (electroplated Cu) substrate to the extent that is able to withstand bending and twisting. The detailed methods include the steps outlined below. After a conventional grinding process, the epitaxial material was directly wet etched from an N-polar GaN surface in an alkaline etchant (KOH) without prelithography. Poly(methyl methacrylate) (PMMA) was then spin coated as sidewall protection for the multiple quantum wells (MQWs). The advanced scheme of electrical interconnection was realized by integrating significantly stretchable MLG with simultaneously high conductivity and optical

Received: December 12, 2013
Published: April 29, 2014

ACS Publications © 2014 American Chemical Society

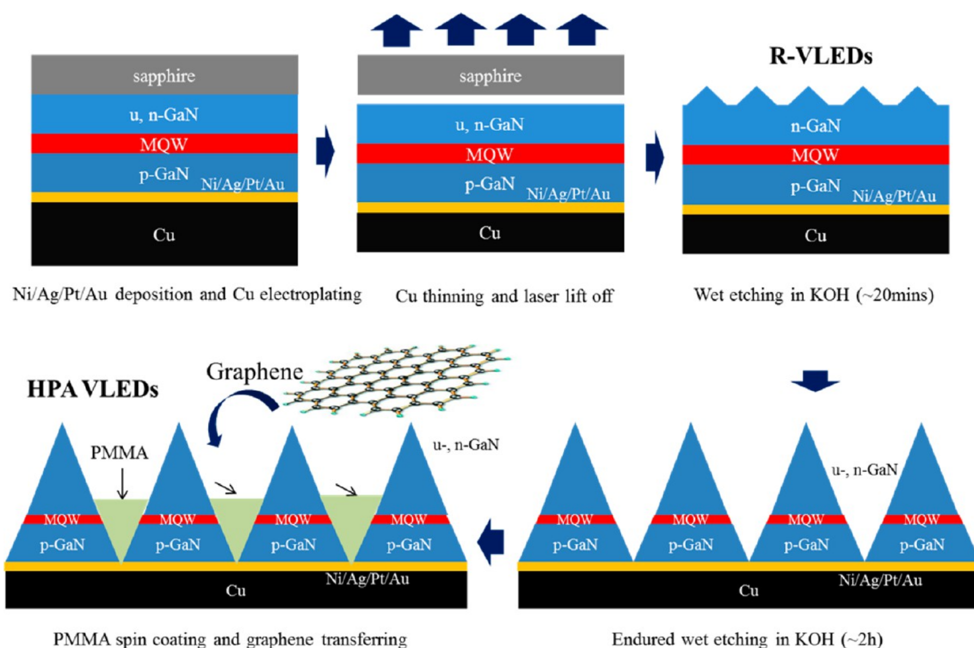

Figure 1. Schematic diagrams of the growth and processing steps of HPA VLEDs.

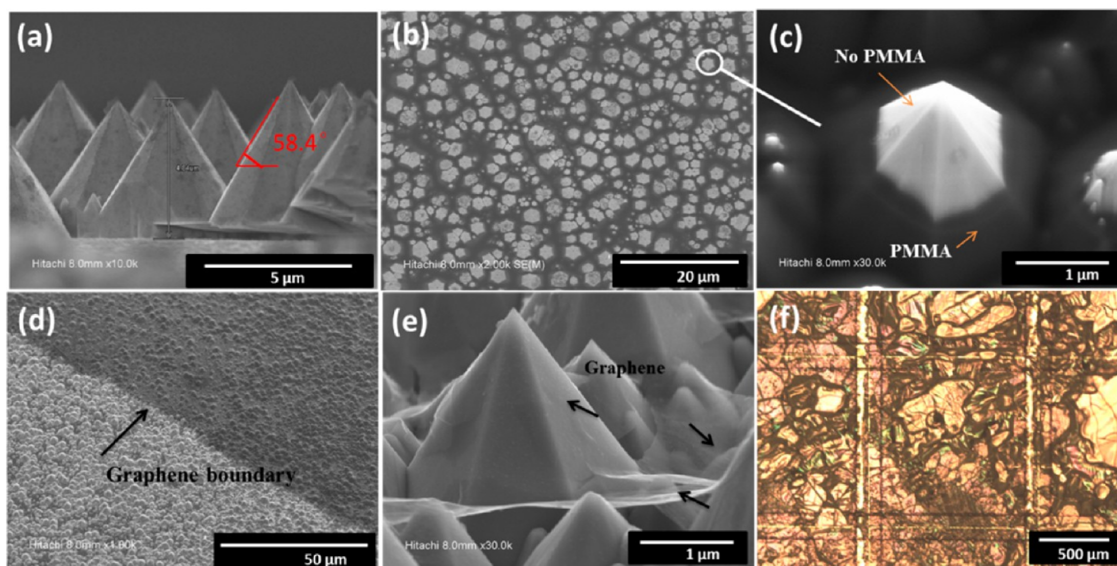

Figure 2. SEM images of HPA VLEDs during each fabrication step: (a) after LLO and 2 h wet etching in KOH; (b, c) after PMMA spin coating and O_2 plasma etching; (d, e) after graphene sheet transfer; and (f) microscopy image of HPA VLEDs with ITO deposited instead of graphene sheets.

transparency. All of the fabrication process steps are based on in situ wafer levels and are completely compatible with conventional VLEDs fabrication technology. Therefore, this scheme will facilitate further system integration; (2) A wet etching process (WEP) of the N-polar GaN showed a dislocation and defect selective mechanism. By eliminating the dislocations and defects (which serve as nonradiative recombination centers) during the WEP, the IQE has been greatly improved. The geometry of the HPA formed after the WEP would increase the LEE as shown by the simulated ray tracing results. Using the dislocation engineering approach to manipulate the dislocation distribution during material epitaxial growth, microscale HPA with improved uniformity, instead of a randomly scattered arrangement, has been achieved after the WEP; (3) The preservation of the microchip functionality after multiple bending cycles was confirmed without impairing the material quality or IQE. By reducing the optical absorption between neighboring pyramids, the LEE was even further improved during bending.

■ HPA VLEDS FABRICATION

Figure 1 schematically draws the processing steps of HPA VLEDs. The material was epitaxially grown on sapphire substrates using a metal organic chemical vapor deposition (MOCVD) method, consisting of a 2 μm unintentionally doped GaN layer (u-GaN), a 2 μm n-type GaN:Si layer (n-GaN), 10 pairs of InGaN/GaN MQWs active layers, and a 0.1 μm p-type GaN/Mg layer (p-GaN). Next, a laser scribbling (LS) process from the p-GaN side was used for the chip configuration, followed by a highly reflective Ni/Ag/Pt/Au

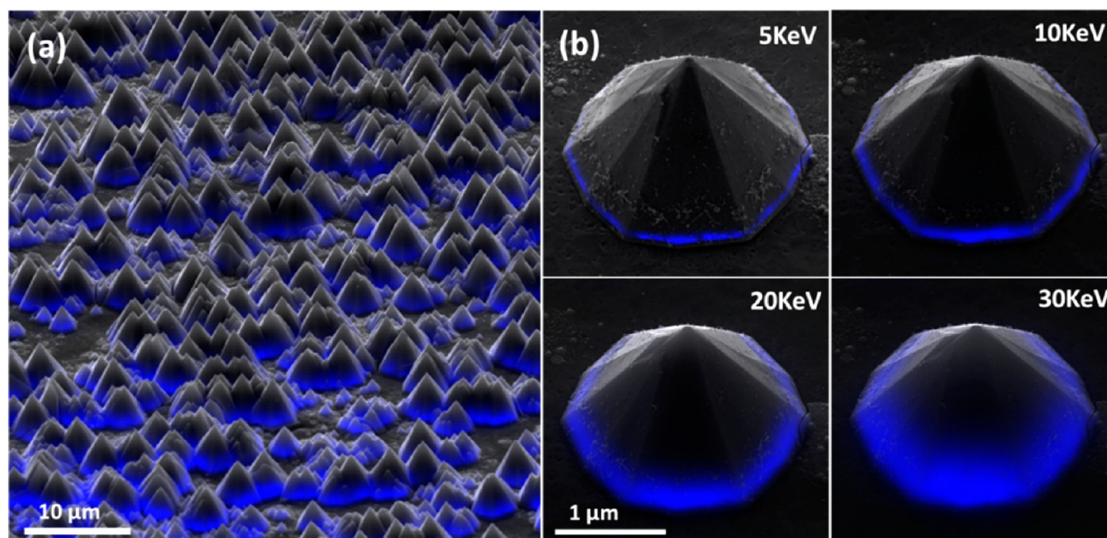

Figure 3. Inclined-view CL images of HPA VLEDs (a) and single pyramid LEDs (b).

(0.5/300/200/2000 nm) p-contact metal deposition on the p-GaN using an electron-beam evaporator (90 °C, 10^{-6} Torr). Cu (100−120 μm) was then electroplated on the Ni/Ag/Pt/Au as the new standing substrate and was further polished and mechanically thinned to approximately 30−50 μm. The thinned Cu substrate is capable of supporting the chip during and after the laser lift off (LLO) process and mechanical deformation. Note that the shear stress between the Cu/Au/Pt/Ag/Ni/GaN layers increases sharply during the Cu thinning process, leading to the possible fatal delamination of each neighboring layer in GaN/Ni/Ag/Pt/Au/Cu and, thus, the ultimate failure of the chip. To avoid this complication, we managed to strengthen the interfacial layer adhesion through the rational adjustment of each fabrication step: (1) slowing down the Cu thinning speed from the default 1 μm/s to approximately 0.3 μm/s with the purpose of decreasing the shear force during the thinning process directly; (2) reducing the Cu electroplating current from 1 A/inch^2 to 0.5 A/inch^2 during the Cu electroplating process, which would decrease the Cu particle size and make the Cu/Au interface more adhesive; (3) increasing the temperature (∼110 °C) and vacuum level of the Au/Pt/Ag/Ni deposition to ensures its reliable adhesion to the p-GaN. We found that 0.5 nm of Ni is the best interfacial adhesion layer.

The epitaxial film displayed the N-polar (000−1) face after the LLO process and was wet etched in 2 mol/L potassium hydroxide (KOH) etchant for ∼2 h at 60 °C, leading to the formation of the HPA. Figure 2a shows scanning electron microscope (SEM) images of the HPA VLEDs. The base radius of a single pyramid is approximately 2−4 μm, showing the hexagonal geometry with a section core angle of ∼58.4°. The pyramid area density is approximately 80% with the MQWs and even the p-GaN layer isolated from each other. In contrast, the pyramids in regular VLEDs (R-VLEDs) are approximately 300−600 nm in base radius and randomly scattered on the surface of the n-GaN. R-VLEDs were etched in the same KOH etchant for ∼20 min. It should be noted that the WEP duration is the only fabrication difference between the HPA VLEDs and R-VLEDs. Figure 1 also shows the R-VLED structure for comparison. The inclined-view cathode luminescence (CL) images of HPA VLEDs and a single HPA VLED are shown in Figure 3, which clearly displays the profile and position of the active region and preserves its function well, even after the wet etching. The monochromatic wavelength corresponds to the emission from the MQWs. Accelerated cathode rays penetrate through the top u-GaN and n-GaN and excite the carriers in the MQWs, which then recombined into visible luminescence. Due to the gradually increased thickness of the u-GaN and n-GaN from edge to center of the pyramid, only carriers in the pyramid periphery, within the cathode penetration depth, are excited. The penetration depth increases with increased cathode ray acceleration voltage.

By PMMA spin coating (4000 r/min, 30 s, PMMA approximately 200 nm thick) and subsequent baking on a hot plate (90 °C, 3 min), the sidewalls of the HPA were protected by insulating PMMA. The PMMA coating on top of each pyramid was then removed using an O_2 plasma process (100 W, 30 s). Figure 2b,c show HPA VLEDs after the O_2 plasma process with the PMMA removed from the top of each pyramid (bright area) and remaining on the areas at the bottom (dark area). The MQWs are located close to the bottom Ni/Ag/Pt/Au; the distance from Ni to MQWs roughly equals the thickness of the p-GaN layer (∼100 nm). By optimizing the O_2 plasma process duration, HPA VLEDs with well-protected MQWs and maximized exposed pyramid areas for subsequent electrical interconnects could be achieved simultaneously and easily. The uniform coating and high controllability over the coating thickness of PMMA, together with its intrinsic transparency and insulation characteristics, make it a useful approach for MQW sidewall protection. The overall exposure of the top n-GaN for each pyramid to O_2, regardless of their size and distribution, makes it applicable for a broad range of fabrications. The lateral dimension of the exposed n-GaN area is approximately 1.5 μm × 1.5 μm. The exposed (no PMMA) and unexposed area (with PMMA) show an obvious brightness contrast under SEM observation. The graphene film, which acts as the electrical interconnection, was grown using the chemical vapor deposition (CVD) method on a Cu (∼20 μm) substrate.[18,20,21,24,25] By dissolving the host Cu substrate in $FeCl_3$, the floated graphene sheets were then transferred onto the HPA VLEDs, which serve as the electrical interconnection.[21−24] Figures 2d,e shows SEM images of HPA VLEDs with transferred graphene sheets. The possible formation of air voids act as potential barriers, resulting in large contact resistance.[25] However, we found that graphene sheets have the ability to

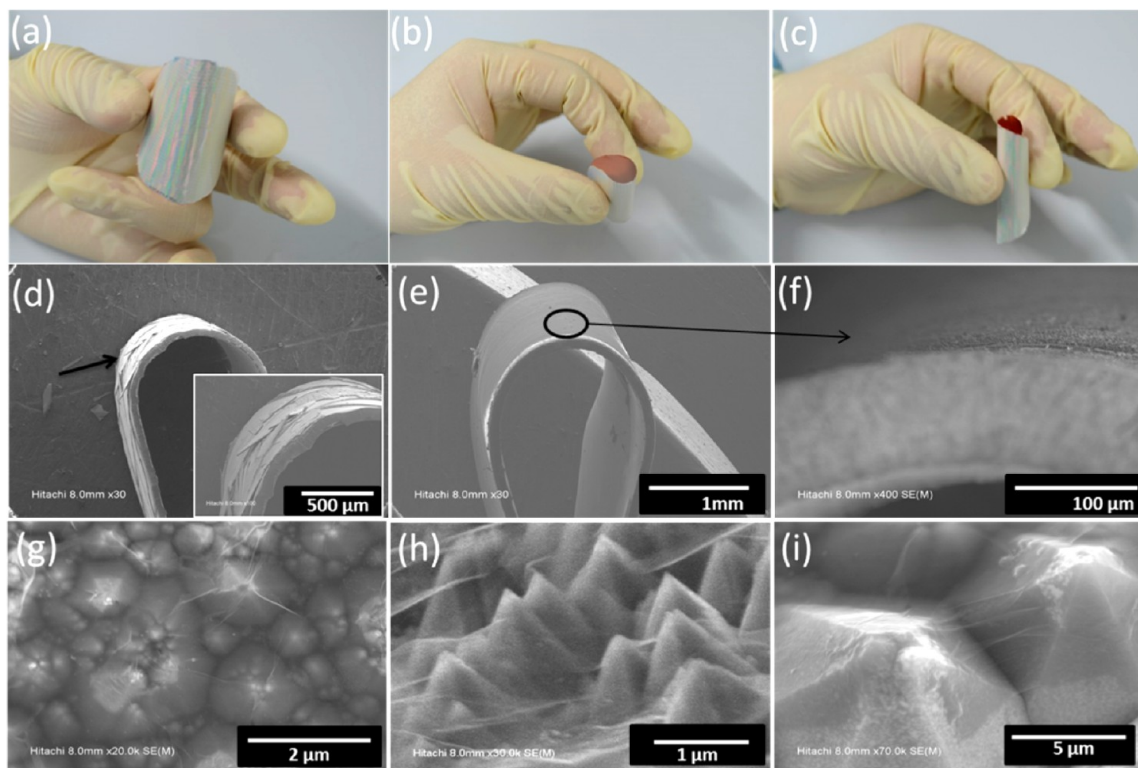

Figure 4. Photographs (a−c) and SEM images (e−i) of bending HPA VLEDs; SEM image of bending R-VLEDs (d).

spontaneously conform to a corrugated surface, as clearly shown in the SEM image of the border areas of the graphene sheets (Figure 2e). A seamless physical contact to deep, recessed device regions in a manner that yields effective contacts and electrical interconnection is of great importance. In contrast, Figure 2f presents the micrograph of HPA VLEDs with ITO on top, demonstrating a very coarse surface over the long-range, which may be ascribed to the elevated temperature during the ITO deposition (~300 °C), leading to the curvature of the Cu substrate. The deposited ITO then becomes nonuniform and even cracked.

The LS and LLO processes could reduce the local stress between the host sapphire substrate and the epitaxial GaN films, while the WEP process further reduces its intrinsic stress. With the isolated microscale pyramids as the building blocks and graphene sheets as the electrical interconnects, HPA VLEDs are able to endure mechanical deformation, that is, bending, twisting, and stretching. Figure 4 show photographs (Figure 4a−c) and SEM images (Figure 4e−i, bending R = 0.5 mm) of outward bending HPA VLEDs. The microscale pyramids were intimately anchored on the mechanically deformed Ni/Ag/Pt/Au/Cu substrate, without any fracturing or peeling, which was confirmed by the magnified SEM image in Figure 4f−i, all of which correspond to the area circled in Figure 4e. For comparison, Figure 4d also shows the R-VLEDs under an almost equal level of bending. It can be seen that the epitaxial GaN layer has been destructively fractured and peeled off into pieces due to the tensile strain results from bending, which further showed the bendability of HPA VLEDs. Figure 4f−i show that the graphene sheets remain continuous after bending. Our graphene sheets consist of multiple layers of graphene that are overlapped and interconnected, which ensures a conducting pathway even if there are cracks or fractures in one of the layers while mechanically deformed. The PMMA coating (approximately 200 nm from the base Ni layer) has a significantly lower Young's modulus than graphene and could stretch to almost the same. The actual multiporous PMMA coating becomes more stretchable as the film internal stress was reduced. It adheres intimately to the sidewall of the pyramids with moderate annealing, even under extreme mechanical deformation. This obvious contrast between bending HPA VLEDs and R-VLEDs clearly indicates the availability of the mechanical deformation of the HPA VLEDs and the significant roles of isolated pyramids arrays and graphene electrical interconnect.

■ BENDING ANALYSIS

The mechanism responsible for graphene's spontaneous conformation to a corrugated surface relies on the low flexural rigidity of graphene, which can lead to a bending energy that is much smaller than the adhesion energy associated with the contact to the GaN, even for substantial relief heights. The total energy U is the sum of the potential energy (W_a) and the bending energy (W_b) as

$$U = -\gamma l_a + \frac{12EIh^2}{a^3} \tag{1}$$

where γ is the work of adhesion between the graphene and GaN, a, $h = a \tan\theta$, and $l_a = a/\cos\theta$ are the base radius, height, and inclined length of the pyramid, respectively. EI is the flexural rigidity of graphene. θ remains constant at approximately 58.4°.[30]

$$\frac{dU}{da} = -\frac{\gamma}{\cos\theta} - \frac{12EI\tan^2\theta}{a^2} < 0 \tag{2}$$

Equation 2 reveals that U decreases, while a increases, which indicates that the minimum energy is reached at the maximum

dx.doi.org/10.1021/ph500133w | ACS Photonics 2014, 1, 421−429

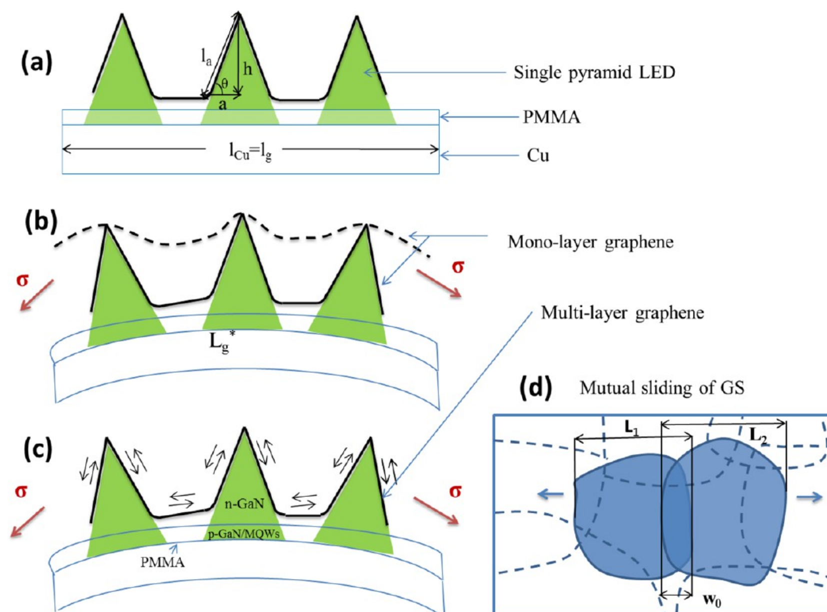

Figure 5. 2D schematic drawings of samples (a) before bending; (b) bending with monolayer graphene as the electrical interconnects; (c) bending with multilayer graphene as the electrical interconnects; (d) neighboring layers in multilayer graphene sliding against each other.

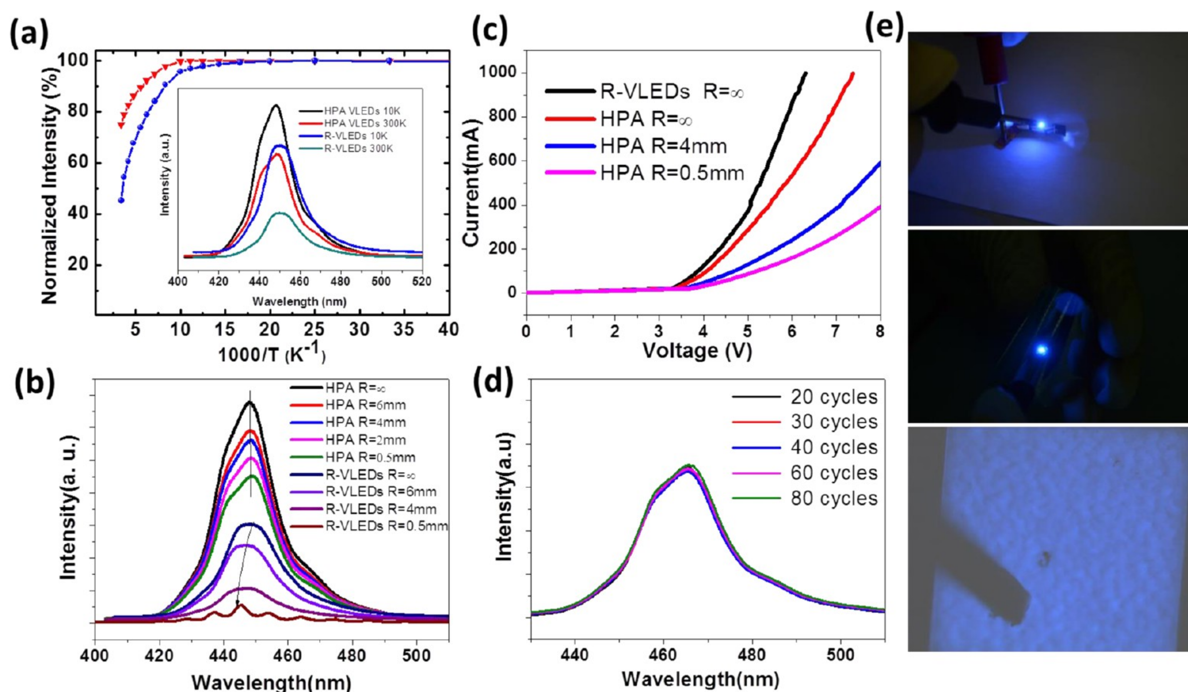

Figure 6. (a) Arrhenius plot of the normalized integral PL intensity of HPA VLEDs and R-VLEDs; the inset of (a) shows the PL spectra of the two samples at 10 and 300 K; (b) PL results of HPA VLEDs and R-VLEDs with different bending radii; (c) Current−voltage characteristics for the flexible VLEDs; (d) PL test results of HPA VLEDs and R-VLEDs with different bending radii; (e) Emission image of 20 mA driven bent and twisted HPA VLEDs.

value of a. The graphene would conform to the roughed surface (corresponding to maximum a) instead of floating on the top of pyramids (corresponding to minimum a), which explains why graphene can spontaneously conform to HPA VLEDs surface. Moreover, it is necessary to investigate the tensile state in graphene during bending. Figure 5 shows a 2D schematic drawing of the samples before (Figure 5a) and after (Figure 5b,c) bending to a radius of R. A single pyramid with a periodic boundary in the plane of the film is considered. l_g*, l_g, and l_{Cu} correspond to the length of strained graphene, pristine graphene, and Cu, respectively; d represents the thickness of Cu; and θ is the section core angle (~58.4°). The graphene is considered to be totally constrained with Cu when bending and l_{Cu} remains constant. Assuming graphene still conforms to the inclined surface of the pyramids with no change in "a" during bending, then the tensile strain and stress in graphene during bending can be simply calculated as the following:

$$\xi = \frac{l_g^* - l_g}{l_g} = \frac{\omega(R+d) - \omega R}{\omega R} = \frac{\omega d}{\omega R} = \frac{d}{R},\ \sigma = E\xi = E\frac{d}{R} \tag{3}$$

$$W_s = \frac{1}{2}\sigma\varepsilon^2 l_g^* = \frac{1}{2}E\left(\frac{d}{R}\right)^3 l_g^* = \frac{1}{2}E\left(\frac{d}{R}\right)^3 \frac{(R+d)l_{Cu}}{R} = \frac{1}{2}E\frac{d^3(R+d)}{R^4}l_{Cu} \tag{4}$$

$$\frac{dW_s}{dR} = -\frac{1}{2}Ed^3\left(\frac{3}{R^4} + \frac{4d}{R^5}\right)l_{Cu} \tag{5}$$

where ε is the strain, σ is the stress, E is Young's modulus of graphene, and W_s is the strain energy of graphene. Equation 5 indicates that W_s increases sharply when R decreases. Additionally, because the Young's modulus, E, of graphene is large (more than 10^6 times PMMA), W_s is dominant compared with W_a and W_b. Graphene will spontaneously release the tensile strain by partially or even totally detaching from the inclined pyramid (Figure S1, Figure 5b). This behavior impairs its function as an electrical interconnect. We circumvent this by using MLG instead of a single layer of graphene (SLG; Figure 5c). Our as-grown graphene is composed of single crystalline graphene sheets with an overlapped region between any two adjacent sheets, as illustrated in Figure 5d. The overlapping width ranges from approximately 50 to 200 nm. The measured sheet size distribution is shown in ref 26 with a mean size of approximately 5 μm. Under tensile strain while bending, the adjacent graphene sheets slide against each other, and the overlapping width will shrink from the initial width, w_0 to $w_0 - L\xi$, where $L = (L_1 + L_2)/2$, L_1 and L_2 are the sizes of the two adjacent graphene sheets. The critical strain that is required to yield separation or "crack" initiation in HPA VLEDs is thus equal to $\xi = \Sigma_{i=1}^{n}(w_0/L_i)$, where n equals the total number of the overlapped region of graphene sheets. Referring to eq 3, at a bending radius of R = 5 mm, the total sliding distances w_0* can be calculated to be 100 nm (for L = 5 μm). Actually, because there are many overlapped regions of graphene sheets, that is, n is quantitatively large, the total sliding distance roughly equals the sum of the sliding width of each adjacent graphene sheet. Thus, the tensile strain can be easily "absorbed and cancelled" by multiple mutual sliding of graphene sheets. Furthermore, the overlapped and interconnected characteristics of the graphene ensure a conducting pathway, even if there are cracks formed in one of the multilayers, perfectly fulfilling its function as the electrical interconnect in HPA VLEDs. The high optical transparency (~85%@550 nm) of graphene sheets ensures less optical loss by absorption. The transmittance versus wavelength plot of MLG is shown in Figure S2, corresponding to 5−6 layered graphene sheets. The sheet resistance of MLG is below 1 KΩ.

IQE AND LEE INVESTIGATION OF HPA VLEDS

The IQEs of HPA VLEDs and R-VLEDs were investigated using the TDPL spectrum. Figure 6a shows the Arrhenius plots of the normalized integral PL intensity of the HPA VLEDs and R-VLEDs. The ratio of the PL intensity at 300 K to that at 10 K is defined as the estimation of IQE. The measured IQE of the HPA VLEDs (~72%) increases by 56% compared with that of R-VLEDs (~48%), which suggests that the HPA VLEDs have an improved crystallinity caused by reductions in dislocations and defects density.[17,30] Furthermore, the temperature at which the PL intensity starts to quench for HPA VLEDs is much higher than that for R-VLEDs. The quenching of the PL intensity for HPA VLEDs can be described well using single activation energy. However, the PL intensity for R-VLEDs first quenches with a weaker activation energy at low temperature, and the second activation energy is dominant at high temperatures. This observation indicates a larger activation energy for the HPA VLEDs, which leads to the restricted activation of nonradiative recombination with increased temperature. The inset in Figure 6a shows the PL spectra of the two samples at 10 and 300 K. The peak intensity of the PL of the HPA VLEDs is 1.6 times stronger than that of R-VLEDs, which may be attributed to the improved IQE and LEE. The theoretically calculated LEE for HPA VLEDs using the ray-tracing method is approximately 58.6%, which is much higher than that of R-VLEDs, ~38.5% (Figure S3). We suppose there are two factors accounting for the improved LEE for HPA VLEDs: total internal reflection (TIR) inhibition by the pyramid shape and guided-mode inhibition due to MQWs isolation. The research of Jun Ho Son et al.[27] revealed that the largest LEE enhancement was realized when the sidewall angle of the nanostructure approaches 23.4° (the critical angle for the TIR at the GaN/air interface is ~23.4°), due to the effective elimination of TIR. The natural sidewall angle of the hexagonal pyramid formed by the WEP in KOH is fixed at ~31.6°,[30] which is close to the critical angle, leading to the inherent improvement in the LEE. Additionally, etching two-dimensional hole arrays that penetrate the MQWs has been theoretically and experimentally shown to be an approach that inhibits light emission into guided modes, thus, increasing LEE.[28,29] This technique can also be applied to HPA VLEDs whose active materials are isolated by endured WEP. Although the removal of the sapphire substrate alleviated the strain between the epilayer and sapphire, the inset in Figure 6a shows that the PL peak wavelength of the HPA V-LEDs still blue shifts by approximately 5 nm compared with the R-VLEDs (at both 10 and 300 K), which could be due to the further reduction in the strain in the epitaxial layer caused by the WEP.

The optical properties of the HPA VLEDs and R-VLEDs with different bending radii have also been investigated using the PL spectra. The measured PL intensity is given by

$$I_d = q\eta_{det}\eta_{ee}\eta_{int}V_n \tag{6}$$

where η_{det}, η_{lee}, η_{int}, and V_n represent the fraction of emitted photons that are collected by the detector, chip LEE, IQE, and the chip excitation area, respectively. During the measurement, the detector distance is kept constant by adjusting the sample stage and the chip is bent to a predesigned curvature using cylindrical molds with different radii. The PL intensity of the flat HPA VLEDs is more than double that of the flat R-VLEDs due to the increased IQE and LEE, which is consistent with the TDPL test. The PL intensity of the HPA VLEDs decreased to ~86.7, ~82.5, and ~71.6% when bending R = 6, 4, and 0.5 mm, respectively. The peak wavelength of the HPA VLEDs is located at 460 ± 2 nm almost independent of the bending radius R, which is different from the R-VLEDs PL whose intensity decreased to ~78.5% at R = 6 mm and almost vanishes when bending to R = 0.5 mm. The peak wavelength of the R-VLEDs blue-shifted from 448.8 to 445.2 nm after bending. The rapidly decaying PL intensity of the R-VLEDs is attributed to the destruction of the epitaxial film (η_{int} approaches to 0). The peak wavelength blue shift results from the further release of intrinsic strain via epitaxial film destruction. As the excitation laser is approximately 150 μm in

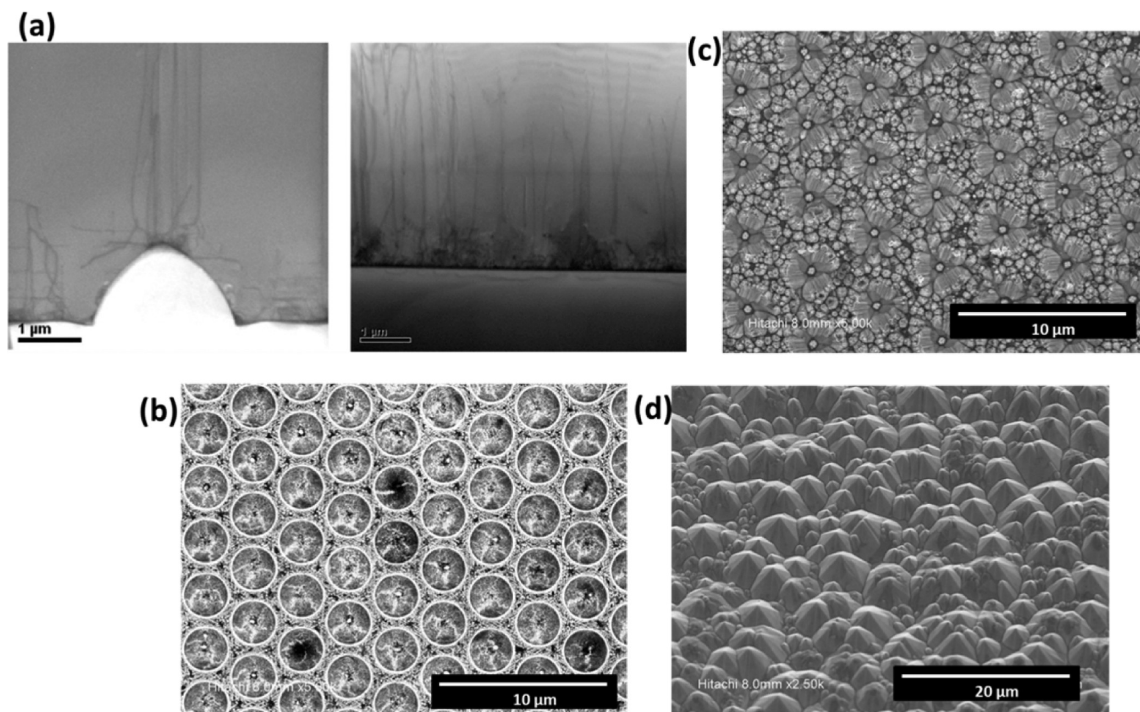

Figure 7. (a) Cross-sectional TEM images of epitaxial LED films grown on PSS (PSS-epi, left) and planar sapphire substrate (right); SEM images of PSS-epi with different process duration in sequence: (b) N-polar u-GaN face after LLO; (c) WEP in 2 mol/L, 50 °C KOH etchant for approximately 1 h; (d) WEP in 2 mol/L, 50 °C KOH etchant for approximately 2 h.

diameter, the V_n in eq 6 is considered constant because light scattering is negligible in such a microsized convex area. The η_{int} of the HPA VLEDs remained constant before and after bending, as the above TDPL results indicated. We have compared the η_{lee} of single hexagonal pyramid LEDs and its corresponding compact array (Figure S3) and found that the single pyramid's η_{lee} is larger (~77.4%) than that of the pyramids arrays (~58.6%), which suggests that some optical modes in one pyramid are reabsorbed by its neighboring pyramids, behaving similarly to interpyramid "guided modes". This result will obviously reduce the η_{lee}. Inspired by this result, we believed bending would somewhat further reduce the "re-absorbing modes" in neighboring pyramids, so that the η_{lee} of the HPA VLEDs could be further improved. Additionally, the optical emission distribution angle is assumed to be expanded during bending. The decreased PL intensity when bending is attributed to the decreased η_{det}. Although the η_{lee} of the bent HPA VLEDs was improved, the expanded optical distribution results in a decreased fraction of emitted photos in the region that can be effectively detected. The reduced PL intensity of the R-VLEDs with bending is attributed to the greatly decreased η_{int}, resulting from the destruction of the epitaxial material. We further investigated the sustainability of the HPA VLEDs using PL tests after bending for different cycles. As shown in Figure 6d, the PL intensity of the HPA VLEDs degrades slightly after 20, 40, 60, and 100 bending cycles, indicating the superior sustainability of HPA VLEDs. Figure 6c presents the current−voltage curves for the HPA VLEDs. The flat HPA VLEDs show degraded forward electrical characteristics (red line, 5.27 V@ 350 mA, 6.23 V@600 mA, and 7.38 V@1000 mA) compared with the flat R-VLEDs (black line, 4.92 V@350 mA, 5.49@600 mA, and 6.3 V@ 1000 mA), which is most likely due to the relatively large contact resistance between the graphene and the inclined pyramids on the n-GaN surface. In contrast to the graphene GaN contacts we reported previously,[8,18,21] in the HPA VLEDs, graphene is mostly deposited on the semipolar $(11\overline{2}\overline{2})$ plane with an angle of ~58.4° to the $(000\overline{1})$ face, as observed from the SEM image in Figure 2a,e. We assume that the different polarizations of the GaN contact crystalline faces have an influence on the forward voltage differences.[8] We also found that the forward voltage (V_F) further increased when the HPA VLEDs were bent. The greater the bend, the more the V_F increased (V_F = 6.76 V, 7.71 V@350 mA with R = 4 mm, 0.5 mm, respectively). Based on the graphene strain sensor research work in our group, we have found that the electrical resistance of graphene woven fabrics increases exponentially with the tensile strain with gauge factors of ~10^3 under 2.6% strains.[26] Excluding the decreased graphene contact area with bending, as discussed above and observed in Figure 4, we also assume that the tensile strain in graphene during bending would cause an increase in its resistance (due to the decreased intrinsic intersection and overlap areas) and, thus, degrade the chip forward electrical characteristics. Figure 6e also shows the emission image of bent and twisted HPA VLEDs driven at 20 mA. From the enlarged micro image shown in the bottom of Figure 6e, the pyramid array feature can be easily observed, which clearly reveals the pyramids array contour.

■ "DISLOCATION ENGINEERING APPROACH" FOR UNIFORM MICROSCALE HPA VLEDS

Serving as the preferential sites for pyramids formation, the random spatial distribution of the threading dislocations leads to the formation of a randomly distributed HPA. Exploring the full potential of the HPA VLEDs would require the development and implementation of efficient and scalable strategies for assembling pyramids into uniform arrays with similar dimensions and spatial layouts. Pattered lithography and dry etching will no doubt lead to an ordered array. However, a

degradation in material quality is inevitably due to the damages caused by the dry etching. Inspired by the dislocation-selective mechanism of the WEP,[30] we conceptually present the "dislocation engineering approach" here for the first time. We demonstrate our first attempt at dislocation distribution manipulation using epitaxial GaN film growth on a pattered sapphire substrate (PSS), which plays a fundamental role in the emergence of an ordered HPA after the WEP. We purchased PSS with a feature size of base × space × height = 2.1 μm × 0.6 μm × 1.5 μm, and the inclined plane was adopted as the epitaxial substrate instead of the planar sapphire used before. An epitaxial film was grown according to the generally adopted two-step method, consisting of a 4 μm u-GaN, a 4 μm n-GaN, 10 pairs of InGaN/GaN MQWs active layers, and a 0.1 μm p-GaN. Figure 7a shows the cross-sectional TEM images of the epitaxial LED films grown on the PSS (PSS-epi, left) and the planar sapphire substrate (planar-epi, right), with a diffraction vector $\mathbf{g} = \bar{2}110$, to display the screw dislocations ($\mathbf{g} \times \mathbf{b} = 0$, $\mathbf{b}$ represents screw dislocation vector (0001)). It is notable to see that the TD density decreased. Furthermore, most of the TDs in the PSS-epi aggregate on the bumps of the PSS and extend to the top layers. The remaining TDs randomly distributed in the regions in between the bumps.[31] In contrast to the PSS-epi, the TDs in the planar-epi randomly spread over the entire region. This phenomenon can be understood by the epitaxial growth mechanisms. For the PSS-epi, the GaN islands nucleated in the region in between the bumps during the low temperature nucleation period and grew larger during the subsequent annealing. The inclined sidewalls of each bump, which have a continuous Miller index, exclude any aggregated GaN nuclei due to the lack of proper nucleation sites. The GaN islands coalesce with neighboring islands on the bumps during the subsequent growth, which leads to the formation of mismatched crystalline interfaces in the form of the TDs, as observed above. Figure 7 also shows SEM images of the N-polar surface of the PSS-epi after etching in 2 mol/L KOH etchant at 50 °C for different times: 0 min (immediately after LLO; Figure 7b); ~1 h (Figure 7c); ~2 h (Figure 7d). The LLO exposed N-polar PSS-epi shows a transfer printed ordered pattern complementary to the PSS. As the WEP process continued, the pattern regularity decreased, showing relatively long-range order and short-range disorder (Figure 7d), which resembles the distribution of the TDs in the PSS-epi. A thinner epitaxial film favors the formation of HPA VLEDs. However, the unique growth mechanism of the PSS-epi (island coalescence and planarization) requires a longer growth time and, thus, makes the typical PSS-epi films thicker than the planar-epi films. Because the PSS-epi film is thicker, it requires a longer WEP time, which would make increase the HPA disorder. Even so, relatively uniform HPA VLEDs with the least active area loss have been obtained. We believe that PSS-based epitaxial growth is an effective way for dislocation distribution manipulation and is beneficial to the spatial site control of HPA VLEDs. Through further growth and WEP parameter optimization, more uniform HPA VLEDs with both performance enhancement (improved IQE and EEE via WEP) and mechanical flexibility are expected.

■ CONCLUSION

To conclude, HPA VLEDs with a ~56% improvement in IQE, ~52% improvement in LEE and intrinsic bendability have been assembled using a rationally designed semiconductor fabrication process. The TDPL tests and ray-tracing simulations confirmed its improved IQE and LEE, respectively. HPA VLEDs with MLG as electrical interconnects can be locally bent, showing stable optical output. The "dislocation engineering approach" has been conceptually presented for long-range ordered microscale HPAs. The results presented here have been established for simple materials and engineering schemes and will motivate the development of flexible optoelectronics, especially flexible inorganic GaN-based LED fabrication.

■ ASSOCIATED CONTENT

Supporting Information

Supplemental Figure 1 shows an SEM image of graphene detaching from an inclined pyramid. Supplemental Figure 2 shows a transmittance versus wavelength plot of a graphene sheet. Supplemental Figure 3 shows the ray-tracing simulation parameters, set up, and light extraction results (LEE) for the HPA VLEDs, R-VLEDs, and a single HP LED. This material is available free of charge via the Internet at http://pubs.acs.org.

■ AUTHOR INFORMATION

Corresponding Authors

*Email: majun@semi.ac.cn.
*E-mail: spring@semi.ac.cn.
*E-mail: hongweizhu@tsinghua.edu.cn.

Notes

The authors declare no competing financial interest.

■ ACKNOWLEDGMENTS

This work was supported by the National High Technology Program of China (Grant No. 2013AA03A101) and the National Natural Science Foundation of China (Grant Nos. 60806001 and 50972067, 61306050 and 61306051).

■ REFERENCES

(1) Rogers, J. A.; Someya, T.; Huang, Y. Materials and mechanics for stretchable electronics. *Science* **2010**, *327*, 1603–7.
(2) Kim, D. H.; Xiao, J.; Song, J.; Huang, Y.; Rogers, J. A. Stretchable, curvilinear electronics based on inorganic materials. *Adv. Mater.* **2010**, *22*, 2108–24.
(3) Nelson, E. C.; Dias, N. L.; Bassett, K. P.; Dunham, S. N.; Verma, V.; Miyake, M.; Wiltzius, P.; Rogers, J. A.; Coleman, J. J.; Li, X.; Braun, P. V. Epitaxial growth of three-dimensionally architectured optoelectronic devices. *Nat. Mater.* **2011**, *10*, 676–81.
(4) Lu, N.; Lu, C.; Yang, S.; Rogers, J. Highly sensitive skin-mountable strain gauges based entirely on elastomers. *Adv. Funct. Mater.* **2012**, *22*, 4044–4050.
(5) Tao, H.; Brenckle, M. A.; Yang, M.; Zhang, J.; Liu, M.; Siebert, S. M.; Averitt, R. D.; Mannoor, M. S.; McAlpine, M. C.; Rogers, J. A.; Kaplan, D. L.; Omenetto, F. G. Silk-based conformal, adhesive, edible food sensors. *Adv. Mater.* **2012**, *24*, 1067–72.
(6) Kuang, D.; Brillet, J.; Chen, P.; Takata, M.; Uchida, S.; Miura, H.; Sumioka, K.; Zakeeruddin, S. M.; Gratzel, M. Application of highly ordered TiO_2 nanotube arrays in flexible dye-sensitized solar cells. *ACS Nano* **2008**, *2*, 1113.
(7) Krebs, F. C.; Gevorgyan, S. A.; Alstrup, J. A roll-to-roll process to flexible polymer solar cells: model studies, manufacture and operational stability studies. *J. Mater. Chem.* **2009**, *19*, 5442.
(8) Wang, L.; Liu, Z.; Guo, E.; Yang, H.; Yi, X.; Wang, G. Interface and transport properties of metallization contacts to flat and wet-etching roughed N-polar n-type GaN. *ACS Appl. Mater. Interfaces* **2013**, *5*, 5797–803.
(9) Liu, Z.; Wei, T.; Guo, E.; Yi, X.; Wang, L.; Wang, J.; Wang, G.; Shi, Y.; Ferguson, I.; Li, J. Efficiency drop in InGaN/GaN multiple-quantum-well blue light-emitting diodes grown on free-standing GaN substrate. *Appl. Phys. Lett.* **2011**, *99*, 091104.

(10) Feezell, D. F.; Speck, J. S.; DenBaars, S. P.; Nakamura, S. Semipolar (20-2-1) InGaN/GaN light-emitting diodes for high-efficiency solid-state lighting. *J. Display Technol. IEEE* **2013**, *9*, 190.
(11) Kim, R. H.; Kim, S.; Song, Y. M.; Jeong, H.; Kim, T. I.; Lee, J.; Li, X.; Choquette, K. D.; Rogers, J. A. Flexible vertical light emitting diodes. *Small* **2012**, *8*, 3123−8.
(12) Nadarajah, A.; Word, R. C.; Meiss, J.; Ko1nenkamp, R. Flexible inorganic nanowire light-emitting diode. *Nano Lett.* **2008**, *8*, 534.
(13) Kim, R. H.; Bae, M. H.; Kim, D. G.; Cheng, H.; Kim, B. H.; Kim, D. H.; Li, M.; Wu, J.; Du, F.; Kim, H. S.; Kim, S.; Estrada, D.; Hong, S. W.; Huang, Y.; Pop, E.; Rogers, J. A. Stretchable, transparent graphene interconnects for arrays of microscale inorganic light emitting diodes on rubber substrates. *Nano Lett.* **2011**, *11*, 3881−6.
(14) Lee, C. H.; Kim, Y. J.; Hong, Y. J.; Jeon, S. R.; Bae, S.; Hong, B. H.; Yi, G. C. Flexible inorganic nanostructure light-emitting diodes fabricated on graphene films. *Adv. Mater.* **2011**, *23*, 4614−9.
(15) Makimoto, T.; Kumakura, K.; Kobayashi, Y.; Akasaka, T.; Yamamoto, H. A vertical InGaN/GaN light-emitting diode fabricated on a flexible substrate by a mechanical transfer method using BN. *Appl. Phys. Express.* **2012**, *5*, 072102.
(16) Tae-il, K.; Rak-Hwan, K.; Rogers, J. A. Microscale inorganic light-emitting diodes on flexible and stretchable substrates. *IEEE Photonics J.* **2012**, *4*, 607−612.
(17) Ma, J.; Wang, L.; Liu, Z.; Yuan, G.; Yi, X.; Ma, P.; Wang, J.; Wang, G.; Li, J. Nitride-based micron-scale hexagonal pyramids array vertical light emitting diodes by N-polar wet etching. *Opt. Exp.* **2013**, *21*, 3547.
(18) Wang, L.; Zhang, Y.; Li, X.; Liu, Z.; Guo, E.; Yi, X.; Wang, J.; Zhu, H.; Wang, G. Partially sandwiched graphene as transparent conductive layer for InGaN- based vertical light emitting diodes. *Appl. Phys. Lett.* **2012**, *101*, 061102.
(19) Chu, C.-F.; Cheng, C.-C.; Liu, W.-H.; Chu, J.-Y.; Fan, F.-H.; Cheng, H.-C.; Doan, T.; Tran, C. A. High brightness GaN vertical light-emitting diodes on metal alloy for general lighting application. *Proc. IEEE* **2010**, *98*, 1197−1207.
(20) Mattevi, C.; Kim, H.; Chhowalla, M. A review of chemical vapour deposition of graphene on copper. *J. Mater. Chem.* **2011**, *21*, 3324.
(21) Wang, L.; Zhang, Y.; Li, X.; Guo, E.; Liu, Z.; Yi, X.; Zhu, H.; Wang, G. Improved transport properties of graphene/GaN junctions in GaN-based vertical light emitting diodes by acid doping. *RSC Adv.* **2013**, *3*, 3359.
(22) Chandramohan, S.; Hye Kang, J.; Katharria, Y. S.; Han, N.; Seon Beak, Y.; Bok, K. K.; Bae Park, J.; Kyu Kim, H.; Suh, E.-K.; Hong, C.-H. Work-function-tuned multilayer graphene as current spreading electrode in blue light-emitting diodes. *Appl. Phys. Lett.* **2012**, *100*, 023502.
(23) Chandramohan, S.; Kang, J. H.; Ryu, B. D.; Yang, J. H.; Kim, S.; Kim, H.; Park, J. B.; Kim, T. Y.; Cho, B. J.; Suh, E. K.; Hong, C. H. Impact of interlayer processing conditions on the performance of GaN light-emitting diode with specific NiO_x/graphene electrode. *ACS Appl. Mater. Interfaces* **2013**, *5*, 958−64.
(24) Zhang, Y.; Wang, L.; Li, X.; Yi, X.; Zhang, N.; Li, J.; Zhu, H.; Wang, G. Annealed InGaN green light-emitting diodes with graphene transparent conductive electrodes. *J. Appl. Phys.* **2012**, *111*, 114501.
(25) Wang, L.; Zhang, Y.; Li, X.; Liu, Z.; Guo, E.; Yi, X.; Wang, J.; Zhu, H.; Wang, G. Interface and transport properties of GaN/graphene junction in GaN-based LEDs. *J. Appl. Phys. D: Appl. Phys.* **2012**, *45*, 505102.
(26) Li, X.; Zhang, R.; Yu, W.; Wang, K.; Wei, J.; Wu, D.; Cao, A.; Li, Z.; Cheng, Y.; Zheng, Q.; Ruoff, R. S.; Zhu, H. Stretchable and highly sensitive graphene-on-polymer strain sensors. *Sci. Rep.* **2012**, *2*, 870.
(27) Son, J. H.; Kim, J. U.; Song, Y. H.; Kim, B. J.; Ryu, C. J.; Lee, J. L. Design rule of nanostructures in light-emitting diodes for complete elimination of total internal reflection. *Adv. Mater.* **2012**, *24*, 2259−62.
(28) Wierer, J. J.; David, A.; Megens, M. M. III-Nitride photonic-crystal light-emitting diodes with high extraction efficiency. *Nat. Photonics* **2009**, *3*, 163−169.
(29) Fan, S.; Villeneuve, P. R.; Joannopoulos, J. D.; Schubert, E. F. High extraction efficiency of spontaneous emission from slabs of photonic crystals. *Phys. Rev. Lett.* **1997**, *78*, 3294−3297.
(30) Wang, L.; Ma, J.; Liu, Z.; Yuan, G.; Yi, X.; Wang, G. N-polar GaN etching and approaches to quasi-perfect micro-scale pyramid vertical light-emitting diodes array. *J. Appl. Phys.* **2013**, *10*, 114 (133101).
(31) Kim, Y. H.; Ruh, H.; Noh, Y. K.; Kim, M. D.; Oh, J. E. Microstructural properties and dislocation evolution on a GaN grown on patterned sapphire substrate: A transmission electron microscopy study. *J. Appl. Phys.* **2010**, *107*, 063501.